Tuning the conversion efficiency of high-order harmonic signals via variation of the Porras factor

B. Ghomashi and A. Becker
JILA and Department of Physics, University of Colorado, Boulder, Colorado 80309-0440, USA

(Received 3 July 2024; revised 13 September 2024; accepted 7 October 2024; published 1 November 2024)

High-order harmonic generation in atomic gases is important for several applications in ultrafast strong-field physics, ranging from attosecond pulse generation to ultrafast spectroscopy and imaging of different forms of matter. In the case of the generation with focused short Gaussian pulses, recent theoretical studies indicate that the conversion efficiency depends on the spatial phase distribution of the driving laser pulse which scales with the Porras factor. Using theoretical analysis and the results of numerical simulations, we find that for positive Porras factors the contribution of the Gouy phase to phase matching can be balanced and the conversion efficiency can be significantly enhanced as compared to a standard laser setup. Specifically, our results indicate that for a Porras factor of $g_0 \simeq 1.2$, the conversion efficiency as well as the cutoff of the harmonic spectra can be optimized while the harmonic lines remain narrow, which may be interesting for spectroscopic applications.

DOI: 10.1103/PhysRevA.110.053101

I. INTRODUCTION

Developments in ultrafast laser technology have been key innovations in the quest of imaging the dynamics of electrons and nuclei in matter on ultrashort timescales as well as performing element-specific measurements in materials with high spatial and temporal resolution. As part of this progress, high-order harmonic generation (HHG) is an important concept and tool [1,2] since it provides the opportunity to convert intense laser light at optical and near-infrared wavelengths into coherent light at vacuum ultraviolet, extreme ultraviolet, and soft-x-ray wavelengths [3]. In the highly nonlinear process which results from the interaction of a gas (or solid) with the electric field of an intense laser pulse, an electron emerges from the atom, propagates in the oscillating field, gathers energy, returns to the core, and upon recombination with the core emits its energy in the form of an ultrashort light pulse [4–8].

For the use of HHG sources in applications, it is beneficial to obtain a high conversion efficiency of the HHG process, a large extent of the harmonic spectrum to high frequencies, and, for certain applications in imaging and spectroscopy [9–14], a narrowness of the harmonic lines. To achieve these goals, an understanding of the coherent buildup of HHG signals from the atoms in the generating medium, i.e., phase matching of the signals, is an important factor [15,16]. One key aspect in the macroscopic process is the spatial phase distribution at the focus of the driving laser pulse. For a monochromatic Gaussian beam there is a π-phase shift across the focus, also commonly known as the Gouy phase [17]. For phase matching in harmonic generation it is often considered, even in experiments with short broadband laser pulses, that the Gouy phase (for a monochromatic beam) has to be compensated by the dipole phase of the harmonics and the dispersion in the neutral gas and by the free electrons. At low ionization levels, the Gouy phase and the dipole phase are known to be the dominant terms, while at higher ionization levels the dispersion terms have an important role, leading to a more elaborate interplay of several phase-matching components [18,19]. More broadly speaking, one may note that the dispersion terms are time-dependent components since the relative ratio of neutrals to free electrons changes during the pulse, while the other terms are components which mainly depend on the spatial location within the laser focus.

Recently, it was pointed out that in focused short Gaussian pulses with a broad frequency spectrum, the carrier-envelope phase of the laser pulses deviates from the Gouy phase [20–23]. Specifically, the carrier-envelope phase of these pulses also varies transversely to the propagation via an additional focal phase term, which scales with the so-called Porras factor g_0 that is specific to the laser setup [21,24]. The study of the impact of the focal phase distribution on strong-field processes induced by short pulses has started recently, for example, in the cases of electron backscattering at metal tips [23], photoelectron spectra (or above-threshold ionization spectra) [25], the generation of high-order harmonics [26–28], and attosecond pulses [29]. Concerning high-order harmonic generation, it has been shown that the focal phase of a short Gaussian pulse is a dominant contribution in phase matching of the harmonic yields, especially in regimes where dispersion effects do not play an important role, e.g., at low intensities and/or low pressures of the generating atomic gas [28]. As a consequence, the efficiency of the harmonic generation appears to depend significantly on the Porras factor.

In order to further understand the role of the Porras factor in high harmonic phase matching, we concentrate on the regime in which dispersion effects due to neutrals and free electrons are negligible. In this way we can study the balance between spatial components due to the carrier-envelope phase (Gouy phase and its short-pulse correction involving the Porras factor) and the harmonic dipole phase. This analysis is of interest for applications of HHG light in spectroscopy and imaging which profit from high conversion efficiencies at low laser pulse intensities as well as from narrow linewidths in view of the potential of element-specific measurements [9–14]. We will however also argue that the results may have an impact for HHG experiments at higher laser

pulse intensities where dispersion terms play a role. Previously, it was predicted that for an experimental setup with a negative Porras factor the best phase-matching conditions are found for a position of a gas jet behind the focal area [27], in agreement with predictions based on the Gouy phase distributions only and typical experimental findings. The impact of the short Gaussian pulse distribution with a negative Porras factor was found in the efficiency and the angular distributions of the harmonic spectrum [26,27].

In the remainder of the present work we aim to show, based on theoretical analysis supported by numerical calculations, that by balancing the contributions to the carrier-envelope phase for a given pulse energy, strong narrow harmonic lines and an extension of the harmonic spectrum can be achieved for focusing conditions and gas jet positions, which are different than in the conventional experimental setup for HHG. More specifically, our results indicate that laser setups with a positive Porras factor provide improved phase-matching conditions for a positioning of the gas jet at the laser focus, as compared to setups with a negative Porras factor. The presentation of our work is organized as follows. In Sec. II we briefly review the contributions to the carrier-envelope phase of a Gaussian pulse and derive an estimate of the Porras factor for an optimum macroscopic buildup of high harmonic generation. In Sec. III we compare these theoretical predictions with the results of numerical calculations. We end with a brief summary in Sec. IV.

II. THEORETICAL CONSIDERATIONS

In this section we first review the main contributions of the carrier-envelope phase of a short Gaussian driving laser pulse, namely, the widely considered Gouy phase and its correction term for a broadband pulse. Next we use the expression for the total focal phase to estimate the optimum Porras factor for an efficient buildup of high harmonic generation at the laser focus, based on the spatial components contributing to the balance.

Assuming a driving laser propagating in the $\hat{z}$ direction, for a short broadband Gaussian distribution the carrier-envelope phase across the focus is given by [21,24]

$$\phi_{\text{pulse}}(z, r) = \phi_{\text{Gouy}}(z) + \phi_{\text{Porras}}(z, r), \tag{1}$$

where

$$\phi_{\text{Gouy}}(z) = -\arctan\left(\frac{z}{z_R}\right) \tag{2}$$

is the Gouy phase for a monochromatic beam and

$$\phi_{\text{Porras}}(z, r) = g_0 \frac{z}{z_R}\left(\frac{1}{1+(\frac{z}{z_R})^2} - \frac{\frac{2r^2}{w_0^2}}{[1+(\frac{z}{z_R})^2]^2}\right) \tag{3}$$

is the correction for a broadband pulse given by Porras [21], where

$$g_0 = \left.\frac{dz_R(\omega)}{d\omega}\right|_{\omega_0} \frac{\omega_0}{z_R(\omega_0)} \tag{4}$$

is the so-called Porras factor. Furthermore,

$$z_R(\omega) = \frac{\omega}{2c} w^2(\omega) \tag{5}$$

is the frequency-dependent Rayleigh range. In all expressions above z and $r = \sqrt{x^2 + y^2}$ are the positions along and transverse to the propagation of the laser and ω_0 is the central frequency of the laser, where $z_R \equiv z_R(\omega_0)$. Finally, $w(\omega)$ is the frequency-dependent input waist at $z = 0$, $w_0 = w(\omega_0)$ is the central frequency beam waist at the focus, and c is the speed of light.

In Fig. 1 we show examples of the geometric focus configurations for three different Porras factors. In each panel the beam waists for different wavelengths are plotted as a function of the propagation distance z, where the origin $z = 0$ is set at the focus. As indicated in one of the panels, in this figure (as well as in all other figures below) it is assumed that the laser pulse propagates from the left to the right. Therefore, negative (positive) values of z correspond to positions before (after) the focus. The three panels correspond to the cases of a negative Porras factor of $g_0 = -1$ in which all colors have the same divergence angle [Fig. 1(a)], a Porras factor of $g_0 = 0$ (Gouy case), in which the Rayleigh length z_R is independent of the laser frequency [Fig. 1(b)], and a positive Porras factor of $g_0 = +1$ with a frequency-independent beam waist at the focus [Fig. 1(c)].

A few methods have been proposed for controlling the Porras factor and the carrier-envelope phase distribution [24,30–33]. Focusing of ultrashort Gaussian pulses can be done using lenses or mirrors; however, a critical factor influencing the carrier-envelope phase distribution is chromatic aberration in the focusing lenses or mirrors, as the Porras factor is sensitive to changes in the Rayleigh length with frequency. The conditions under which focusing via lenses and mirrors can be achieved without distortion have been discussed [24,30–32]. An alternative way to spatial manipulation of the carrier-envelope phase is via pulse chirping, which introduces variations in the phase distribution that can be leveraged to control flat phase regions of the pulse [24,33].

The standard geometry of a few-cycle laser system based on a hollow-core fiber compressor used for high-order harmonic generation corresponds to negative Porras factors [25]. More specifically, for such a laser setup a Porras factor of $g_0 \approx -2$ was determined in a recent experiment [23]. For such a geometry, optimal phase-matching conditions occur for positions of the gas jet after the laser focus, similarly to the Gouy phase distribution ($g_0 = 0$) [27]. However, it can be expected and it has been shown recently [26,28] that the efficiency of the high-order harmonic process depends on the Porras factor. In view of our goal to determine the Porras factor for an optimal coherent buildup of harmonic radiation, we are aiming for a large region of slow phase variation in the region of highest intensity, i.e., at the laser focus.

To get insight into how such a setup can be realized, we first perform a Taylor expansion of the carrier-envelope phase distribution ϕ_{pulse} [Eq. (1)] as a function of $Z = z/z_R$ and $R = r/w_0$, which yields

$$\phi_{\text{pulse}}(Z, R) = \sum_{n=1}^{\infty} (-1)^n \left(\frac{1}{2n-1} - g_0(1 - 2nR^2)\right) Z^{2n-1}. \tag{6}$$

We note that, near the focus, i.e., for R and Z small, the first-order term ($n = 1$) of the expansion dominates. We further

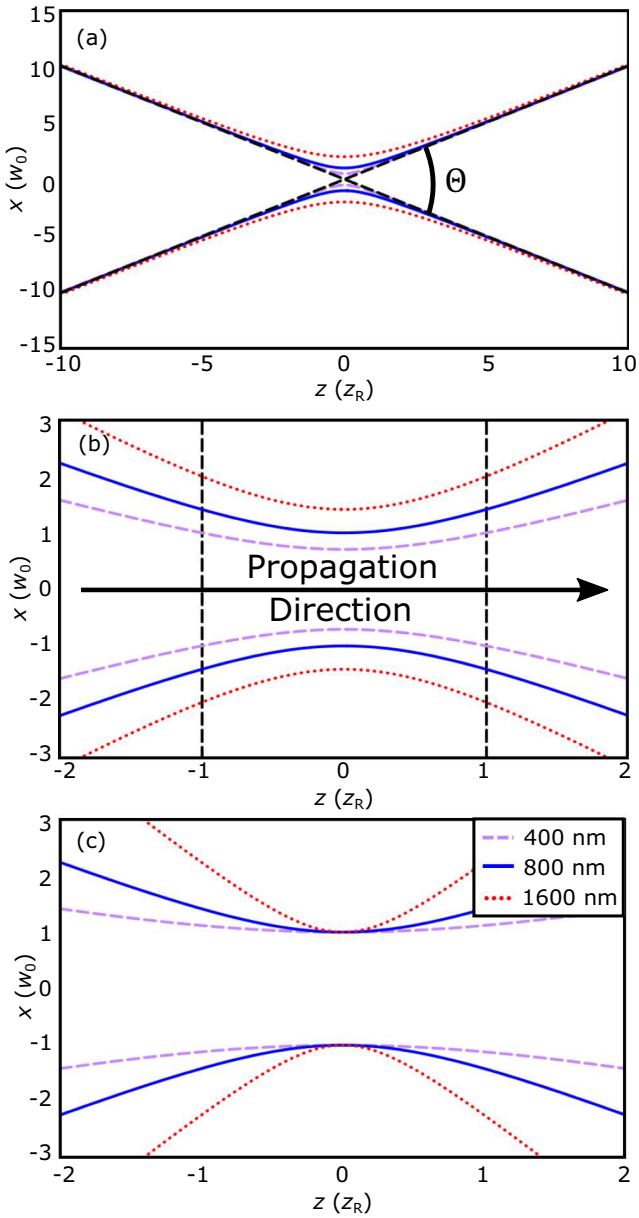

FIG. 1. Three characteristic geometric focus configurations for a short Gaussian laser pulse with (a) a negative Porras factor $g_0 = -1$, (b) a Porras factor of $g_0 = 0$ (Gouy case), and (c) a positive Porras factor $g_0 = 1$. The curves represent the beam waist as a function of the propagation distance given by z and the transversal distance $x = \sqrt{1+z^2}$ (where x and z are scaled in units of the central-frequency beam waist w_0 and the Rayleigh length z_R; see the text for details) for three example wavelengths (400 nm, purple dashed line; 800 nm, blue solid line; and 1600 nm, red dotted line). Note that in this figure as well as in all other figures below the propagation direction of the laser pulse is assumed to be from left to the right. The origin of the propagation direction, $z = 0$, is set at the focus; negative (positive) values of z correspond to positions before (after) the focus.

observe that if g_0 is taken to be negative, as is the case for a conventional high-order harmonic setup [25], the magnitude of the coefficient in the bracket grows as a function of g_0, leading to strong variations in ϕ_{pulse} and hence unfavorable phase-matching conditions near the focus. This is in agreement with common experimental knowledge, which leads to a position of the gas jet behind the focus in such experiments. In contrast, if g_0 is positive, the two terms in the brackets have opposite sign and therefore tend to cancel. Thus, we expect smaller phase variations at the focus in this case. Indeed, restricting the expansion to the first-order term and setting $R = 0$, we get $g_0 = 1$ as an estimate for the Porras factor for optimum phase matching at the focus. As discussed above, a Porras factor $g_0 = 1$ corresponds to a beam with a frequency-independent beam waist [25] [see Fig. 1(c)]. We may note that a laser focusing configuration with a positive Porras factor of $g_0 = 0.4$ has been realized recently via pulse chirping [33].

III. NUMERICAL RESULTS AND DISCUSSION

A. Numerical methods and parameters

We next compare our theoretical predictions with the results of numerical calculations. To this end, we performed model simulations of macroscopic high-harmonic generation without performing a full spatial-temporal pulse propagation. The single-atom response for a hydrogen atom interacting with an intense laser pulse was obtained by solving the respective time-dependent Schrödinger equation (TDSE). In these calculations the electric field of the laser pulse was taken to be linearly polarized in the $\hat{y}$ direction and obtained via $E_y(t) = -\frac{1}{c}\frac{\partial}{\partial t}A(t)$ from the vector potential

$$A(t) = A_0 \sin^2\left(\frac{\pi t}{\tau}\right)\sin(\omega t + \phi), \tag{7}$$

where $A_0 = \frac{c\sqrt{I}}{\omega_0}$, $\tau = \frac{2\pi N}{\omega_0}$, I is the peak intensity, ϕ is the carrier-envelope phase, and N is the number of cycles in the pulse (full width). The laser-electron interaction is represented in the velocity gauge. To propagate the wave function in the presence of the electric field, we follow the strategy outlined in Refs. [34,35].

The angular part of the wave function is expanded in 15 spherical harmonics and the radial part of the wave function expanded in a basis of eighth-order B splines. One hundred thirty nodes are placed such that the spacing between nodes is quadratic near the origin and then becomes constant at a chosen radius (here 30 a.u.) to increase the resolution near the origin. The wave function is propagated in a box with a maximum radial extent of 100 a.u. For the solution of the TDSE, we use the Crank-Nicolson method to propagate the wave function starting from the initial state with a time step $dt = 0.2$ a.u. As an absorbing boundary, we use exterior complex scaling [36], where the edge of the grid (10%) is rotated into complex space by an angle $\eta = \pi/16$. To obtain the HHG spectra, the dipole acceleration $a(t)$ is evaluated using the Ehrenfest theorem

$$a(t) = \left\langle -\frac{\partial}{\partial y}\left(-\frac{1}{\rho}\right)\right\rangle \tag{8}$$

and the complex harmonic response $a(\Omega)$ is then obtained by taking the Fourier transform of the dipole acceleration. The harmonic power spectra $S(\Omega)$ is the absolute square of $a(\Omega)$. For all calculations in this work the spatial profile of the laser is chosen to be a Gaussian beam with a beam waist of $w_0 =$

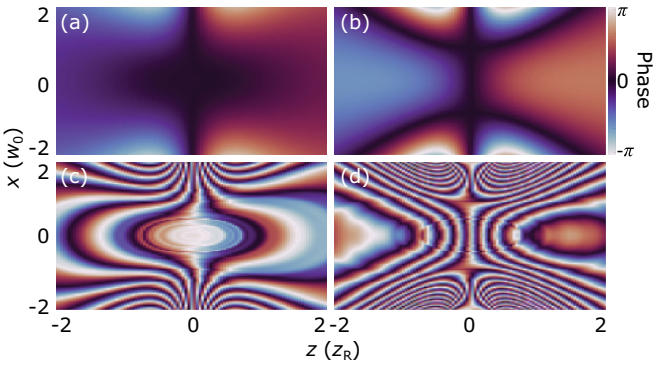

FIG. 2. Gaussian pulse phase for Porras factor (a) $g_0 = 1$ and (b) $g_0 = -2$ and total phase distribution of harmonic 13 for Porras factor (c) $g_0 = 1$ and (d) $g_0 = -2$.

30 μm (Rayleigh length $z_R \approx 3500$ μm),

$$I(r,z) = I_0(1+Z^2)^{-1}\exp\left(-\frac{2R^2}{1+Z^2}\right), \tag{9}$$

where all symbols are defined near Eqs. (5) and (6). Furthermore, we consider a wavelength of the driving laser of 800 nm and a duration of 20 optical cycles. If not stated differently, the macroscopic results shown below are obtained for a peak intensity of 1.2×10^{14} W/cm^2.

To determine the macroscopic signal at the detector, we use the discrete dipole approximation as in Ref. [37]. In this approach the continuous medium is approximated by the distribution of a number of individual emitters. The macroscopic yield is then obtained as a superposition of the fields generated by the emitters. In particular, the total field at a detector located at $\mathbf{R}_d$ generated by atoms located at $\mathbf{R}_j$ ($j = 1, 2, 3, \ldots$) is given by

$$\mathbf{E}(\mathbf{R}_d,\omega) = \frac{1}{c^2|R_d|}e^{-i(\omega/c)|R_d|}\sum_j \mathbf{a}_j(\Omega)e^{-i(\omega/c)[\mathbf{R}_j\cdot(\hat{R}_d-\hat{Z})]}, \tag{10}$$

where $\mathbf{a}_j(\omega)$ is the microscopic HHG signal obtained from solving the TDSE for the jth atom.

Single-atom responses have been evaluated via a nearest-neighbor algorithm from a set of *ab initio* TDSE results over an intensity range from 1.2×10^{12} to 2.0×10^{14} W/cm^2 (with $\Delta I = 1.488 \times 10^{11}$ W/cm^2). The convergence of the results with respect to the intensity spacing has been tested. We note that alternatively in this model macroscopic results can also be obtained using an interpolation algorithm [26,38]. This approximation to the full Maxwell solution relies on the dipole approximation and the assumption that the generated radiation does not interact with the medium. While the model does not consider the full spatiotemporal pulse propagation through the medium, it can provide insights into the relative importance of spatial contributions in the phase-matching process.

B. Impact of the Porras factor on efficient coherent macroscopic high-order harmonic generation

In Fig. 2 we compare the Gaussian pulse phase ϕ_{pulse} [Figs. 2(a) and 2(b)] and the phase distribution of the 13th harmonic [Figs. 2(c) and 2(d)] for two values of the Porras factor, namely, the estimated value $g_0 = 1$ for optimized phase matching at the focus [Figs. 2(a) and 2(c)] and the value $g_0 = -2$ for the conventional laser setup in the case of HHG [Figs. 2(b) and 2(d)]. The effect of ϕ_{pulse} on the laser-induced dipole phase $\Phi_{\text{dip}}(\Omega, \phi_{\text{pulse}})$ is approximated by [37]

$$\Phi_{\text{dip}}(\Omega;\phi_{\text{pulse}}) = \Phi_{\text{intrinsic}}(\Omega) + H(\Omega)\phi_{\text{pulse}}, \tag{11}$$

where $\Phi_{\text{intrinsic}}(\Omega)$ is the intrinsic phase of the single-atom HHG response at frequency Ω and $H(\Omega)$ is the harmonic number rounded to the nearest odd integer. From the comparison one sees that for the estimated optimum Porras factor $g_0 = 1$[Figs. 2(a) and 2(c)] a region with a flat phase distribution occurs in the focal region, while in the conventional setup for $g_0 = -2$ [Figs. 2(b) and 2(d)] a region with small phase variations is found behind the focus. This confirms the results of the theoretical estimate above, while for $g_0 = -2$ it agrees with previous results (e.g., [27]).

Next we investigate the properties of the generated high harmonic signals. To this end, we consider several aspects and respective measures to quantify the results and conclusions: (i) the strength of the harmonic signal which we measure by integrating the generated radiation around a harmonic order $\Omega = N\omega$ [27],

$$M_{g_0}^{(N)} = \int_{(N-\delta)\omega_0}^{(N+\delta)\omega_0} S(\Omega)d\Omega, \tag{12}$$

where $S(\Omega)$ is the macroscopic radiation signal and we have chosen $\delta = 0.25$ in our analysis; (ii) the extent of the harmonic spectrum, i.e., the cutoff which we analyze by comparing harmonic spectra; and (iii) the narrowness of the harmonic lines which we analyze via a sideband measure given by [27]

$$\mathcal{S}_{g_0}^{(N)} = \frac{\int_{(N-\delta)\omega_0}^{(N+\delta)\omega_0} S(\Omega)d\Omega}{\int_{(N-1)\omega_0}^{(N+1)\omega_0} S(\Omega)d\Omega - \int_{(N-\delta)\omega_0}^{(N+\delta)\omega_0} S(\Omega)d\Omega}. \tag{13}$$

We note that as the value of $\mathcal{S}_{g_0}^{(N)}$ increases, more radiation is concentrated at the Nth harmonic line. To perform the analysis we fix the peak intensity and pulse duration, i.e., the pulse energy, and assume gas jets with a Gaussian density distribution along z, centered about z_{off}, with a width of $\sigma_z = 800$ μm $\approx 0.23 z_R$, and constant density along x (the radial direction):

$$\rho(x,y,z) = \rho_0 \exp\left(-\frac{(z-z_{\text{off}})^2 + y^2}{2\sigma_z^2}\right). \tag{14}$$

Furthermore, we consider a low gas density of $\rho_0 = 10^{18}$ cm^{-3}, which corresponds to 40.4 mbar using an ideal gas law at 20 °C.

We first consider an important quantity in harmonic generation, namely, the efficiency of the generation. To this end, we compare in Fig. 3 the relative strength of three different harmonics, a below-threshold harmonic $N = 7$ [Fig. 3(a)] and two plateau harmonics $N = 13$ [Fig. 3(b)] and $N = 19$ [Fig. 3(c)], as a function of the offset position of the gas jet z_{off} (horizontal axis) and the Porras factor g_0 (vertical axis). The comparison reveals that overall the strongest harmonics are generated for $g_0 \simeq 1$ and positioning of the gas jet in the focal region of high intensity. Furthermore, other

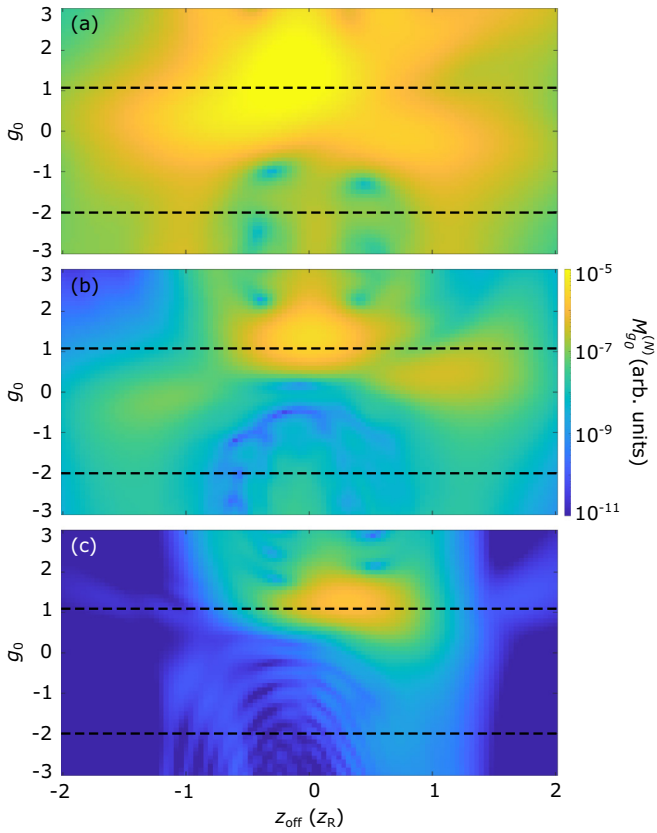

FIG. 3. Integrated signal strength $M^{(N)}_{g_0}$ [Eq. (12)] for three harmonics, (a) the 7th harmonic, (b) the 13th harmonic, and (c) the 19th harmonic, as a function of the Porras factor and the position of the gas jet. The parameters of the driving laser are a wavelength of 800 nm, a duration of 20 optical cycles, and a peak intensity of 1.2×10^{14} W/cm^2.

general trends, discussed earlier, are also confirmed. For positive Porras factors phase-matching conditions are in general most favorable near the focus. In contrast, for negative Porras factors (including the standard setup with $g_0 = -2$) the impact of the Porras factor leads to unfavorable phase matching at the focus. The best conditions and the strongest harmonics for negative Porras factors are found for a gas jet location after the focus.

From the results we see that the optimal Porras factor for phase matching at $z = 0$ is $g_0 \approx 1.2$, which is slightly larger than the value of $g_0 = 1$ which we estimated via a Taylor approximation for optimal phase matching at the central point ($z = 0, r = 0$). This is evidence of the circumstance that the coherent buildup occurs not just at one point but in volume around the focal point. Restricting the expansion in Eq. (6) to the first-order term, we note that for $g_0 = 1.2$ the term is equal to zero at $R = r/w_0 \approx \pm 0.29$, which corresponds to 17% of the full width at half maximum of the Gaussian intensity distribution at the focus ($z = 0$). This is an indication of the size of the coherent focal volume.

It can be expected that a favorable phase matching in the region of highest intensities also leads to an extension of the plateau of the harmonic spectrum since it is known that the cutoff scales with the intensity (e.g., [6]). We exemplify

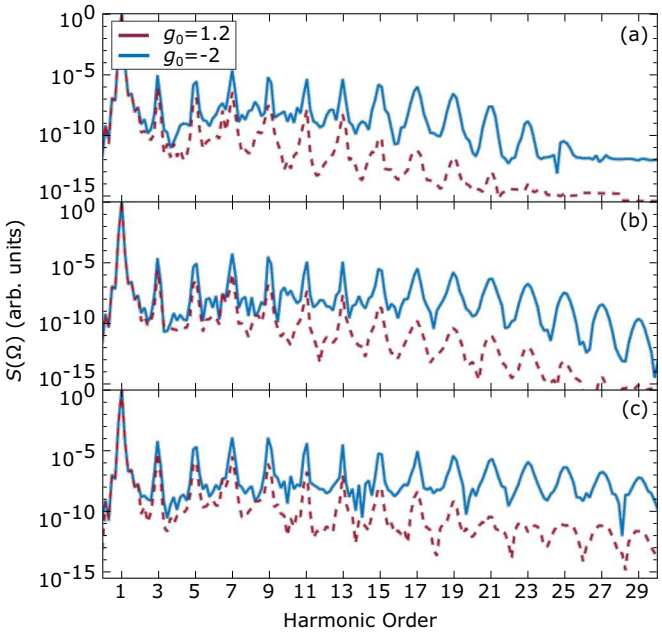

FIG. 4. Comparison of high-order harmonic spectra for the optimum Porras factor $g_0 = 1.2$ (blue solid line) and the Porras factor for the standard laser setup $g_0 = -2$ (red dashed line) for peak intensity (a) $I = 8 \times 10^{13}$ W/cm^2, (b) $I = 1.2 \times 10^{13}$ W/cm^2, and (c) $I = 2 \times 10^{13}$ W/cm^2. In each case the gas jet position for optimum conversion efficiency has been chosen.

this in Fig. 4, where we compare the harmonic spectra for $g_0 = 1.2$ and -2 for three different peak intensities, namely, 8.0×10^{13} W/cm^2 [Fig. 4(a)], 1.2×10^{14} W/cm^2 [Fig. 4(b)], and 2.0×10^{14} W/cm^2 [Fig. 4(c)]. In all cases we have chosen gas jet positions for optimum phase matching, i.e., $z_{off} = 0$ for $g_0 = 1.2$ and $z_{off} = 0.9\ z_R$ for $g_0 = -2$. The comparison confirms the enhancement of the harmonic signals throughout the spectrum as well as the extension of the plateau by a few harmonics in the case of the optimum Porras factor.

To further validate and quantify the enhancement of the conversion efficiency, we present in Fig. 5 the ratio of the signal strengths for the two Porras factors at the optimum gas

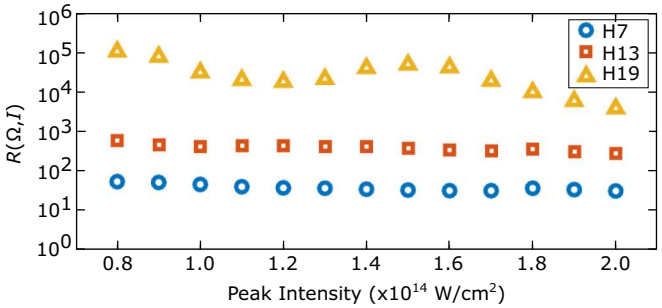

FIG. 5. Ratio of the signal strength $R(\Omega, I)$ [Eq. (15)] at $g_0 = 1.2$ as compared to $g_0 = -2$ for three harmonics, the 7th harmonic (circles), the 13th harmonic (squares), and the 19th harmonic (triangles), as a function of the peak intensity. In all cases the gas jet is positioned at the optimal position, i.e., $z = 0$ and $z = 0.9 z_R$, respectively.

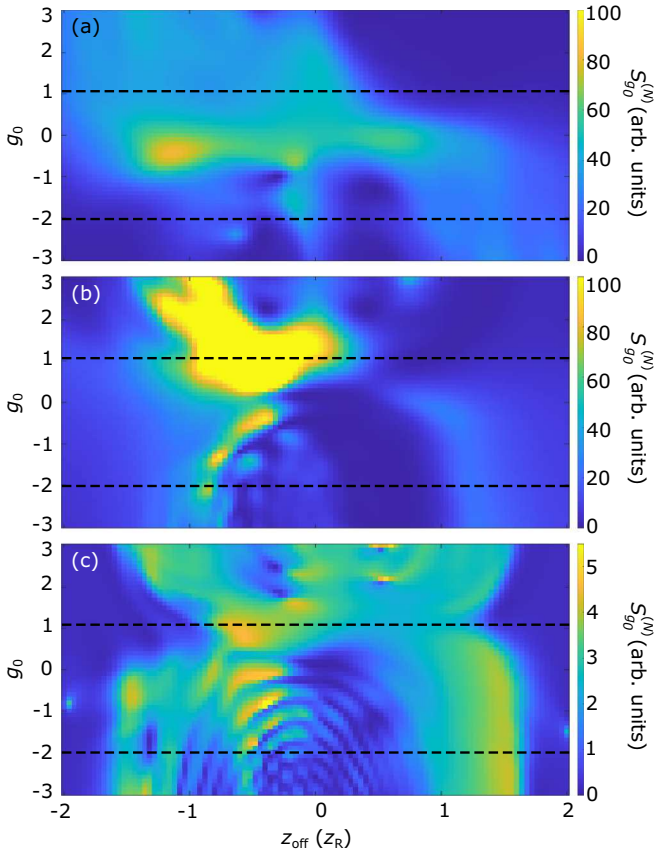

FIG. 6. Sideband measure $\mathcal{S}_{g_0}^{(N)}$ [Eq. (13)] for three harmonics, (a) the 7th harmonic, (b) the 13th harmonic, and (c) the 19th harmonic, as a function of the Porras factor and the position of the gas jet.

jet positions, i.e.,

$$R(\Omega, I) = \frac{M_{g_0=1.2}^{(N)}(\Omega)}{M_{g_0=-2}^{(N)}(\Omega)}, \tag{15}$$

at three harmonics $\Omega = 7\omega_0$ (circles), $\Omega = 13\omega_0$ (squares), and $\Omega = 19\omega_0$ (triangles) as a function of the peak intensity. The enhancement of two to four orders of magnitude may be interesting for spectroscopic applications of harmonics [9–14] in regimes in which diffraction effects by neutrals and free electrons do not play a role.

It is interesting to note that another aspect, namely, the narrowness of the harmonic lines, which is important concerning the application of such light for certain studies in imaging and spectroscopy [9–14], remains intact for the generation of high-order harmonics with an experimental setup represented by a positive Porras factor. The comparison in Fig. 4 shows that in the case of $g_0 = 1.2$ the harmonic lines are narrow and have a good contrast of harmonic signal to off-harmonic yield; indeed, these aspects are rather similar to the standard laser setup for high-order harmonic generation ($g_0 = -2$). To further confirm this observation, we present in Fig. 6 the sideband measure (13) as a function of the position of the gas jet $z_{\rm off}$ and the Porras factor g_0. As for the harmonic signal strengths, we indeed observe that near the focus for Porras factors of $g_0 \simeq 1.2$ the sideband measure is large. This indicates a concentration of the radiation at the harmonic and hence a high contrast ratio between the harmonic line and the off-harmonic radiation, which is a favorable aspect for spectroscopic applications [9–14].

IV. CONCLUSION

In summary, via results of theoretical analysis and numerical calculations, we have shown that the phase-mismatch contribution by the Gouy phase can be balanced by a correction term to the carrier-envelope phase for short broadband Gaussian laser pulses, which scales with the Porras factor. In regimes in which these terms, as well as the harmonic dipole phase, are dominant for phase matching, the generation of high-order harmonic signals in atomic gases can be optimized by varying the Porras factor. As compared to the standard laser setup used for harmonic generation, which corresponds to a negative Porras factor $g_0 = -2$, the efficiency of the yields and the extension of the harmonic spectrum can be significantly enhanced for positive Porras factors, with an optimum value of about $g_0 \simeq 1.2$. In a different context, a focusing configuration with a positive Porras factor $g_0 = 0.4$ has been realized recently via pulse chirping [33].

Since the theoretical analysis and the computations in the present study were obtained without taking dispersion effects during the high harmonic process into account, the results are in particular relevant in the regime of low laser pulse intensities and/or low gas densities. Therefore, the results should be most interesting for certain recent applications of high harmonic generation in imaging and spectroscopy [9–14]. Such applications would likely profit from the combination of a significant increase in conversion efficiency while retaining narrow linewidths. However, one may argue that the present results also provide some alternative ideas for efficient high-order harmonic generation at higher laser intensities, including the generation of attosecond pulses. The terms considered in the present study are spatial contributions in the phase-matching process and the results indicate that a balance of these components can be achieved near the focus for a laser setup with a positive Porras factor. On the other hand, the dispersion terms, which are not considered, depend on the relative number of neutrals and charged particles, which do change over the course of the laser pulse. Thus, a balance of the dispersion terms may be achieved transiently in some time window during the pulse, independent of the optimum spatial location. Of course, these thoughts consider the elaborate phase-matching process in a simplified way only; however, the results may still indicate that an exploration of an alternative route for efficient high harmonic generation even at high intensities could be of interest. A confirmation of such thoughts would require either an experimental observation or a numerical study taking the full spatiotemporal phase-matching process into account, which is beyond the scope of the present work.

ACKNOWLEDGMENTS

We thank Dr. M. Murnane and Dr. H. Kapteyn for many discussions and valuable insights concerning the microscopic and macroscopic aspects of high-order harmonic generation.

We would also like to thank the anonymous reviewers of this paper for their constructive feedback, which helped us to refine the presentation of the scope and potential impact of the work. This work was primarily supported by the U.S. National Science Foundation through Grant No. PHY-2207995. We also acknowledge the use of computing resources in part supported by the U.S. National Science Foundation through Grant No. PHY-2317149.

[1] A. McPherson, G. Gibson, H. Jara, U. Johann, T. S. Luk, I. A. McIntyre, K. Boyer, and C. K. Rhodes, Studies of multiphoton production of vacuum-ultraviolet radiation in the rare gases, J. Opt. Soc. Am. B **4**, 595 (1987).

[2] M. Ferray, A. L'Huillier, X. F. Li, L. A. Lompre, G. Mainfray, and C. Manus, Multiple-harmonic conversion of 1064 nm radiation in rare gases, J. Phys. B **21**, L31 (1988).

[3] T. Popmintchev, M.-C. Chen, D. Popmintchev, P. Arpin, S. Brown, S. Ališauskas, G. Andriukaitis, T. Balčiunas, O. D. Mücke, A. Pugzlys, A. Baltuška, B. Shim, S. E. Schrauth, A. Gaeta, C. Hernández-García, L. Plaja, A. Becker, A. Jaron-Becker, M. M. Murnane, and H. C. Kapteyn, Bright coherent ultrahigh harmonics in the keV x-ray regime from mid-infrared femtosecond lasers, Science **336**, 1287 (2012).

[4] K. J. Schafer, B. Yang, L. F. DiMauro, and K. C. Kulander, Above threshold ionization beyond the high harmonic cutoff, Phys. Rev. Lett. **70**, 1599 (1993).

[5] P. B. Corkum, Plasma perspective on strong field multiphoton ionization, Phys. Rev. Lett. **71**, 1994 (1993).

[6] M. Lewenstein, P. Balcou, M. Y. Ivanov, A. L'Huillier, and P. B. Corkum, Theory of high-harmonic generation by low-frequency laser fields, Phys. Rev. A **49**, 2117 (1994).

[7] P. M. Paul, E. S. Toma, P. Breger, G. Mullot, F. Augé, P. Balcou, H. G. Muller, and P. Agostini, Observation of a train of attosecond pulses from high harmonic generation, Science **292**, 1689 (2001).

[8] M. Hentschel, R. Kienberger, C. Spielmann, G. A. Reider, N. Milosevic, T. Brabec, P. Corkum, U. Heinzmann, M. Drescher, and F. Krausz, Attosecond metrology, Nature (London) **414**, 509 (2001).

[9] D. Zusin, P. M. Tengdin, M. Gopalakrishnan, C. Gentry, A. Blonsky, M. Gerrity, D. Legut, J. M. Shaw, H. T. Nembach, T. J. Silva, P. M. Oppeneer, H. C. Kapteyn, and M. M. Murnane, Direct measurement of the static and transient magneto-optical permittivity of cobalt across the entire *M*-edge in reflection geometry by use of polarization scanning, Phys. Rev. B **97**, 024433 (2018).

[10] P. D. Baksh, M. Ostrčil, M. Miszczak, C. Pooley, R. T. Chapman, A. S. Wyatt, E. Springate, J. E. Chad, K. Deinhardt, J. G. Frey, and W. S. Brocklesby, Quantitative and correlative extreme ultraviolet coherent imaging of mouse hippocampal neurons at high resolution, Sci. Adv. **6**, eaaz3025 (2020).

[11] W. Eschen, L. Loetgering, V. Schuster, R. Klas, A. Kirsche, L. Berthold, M. Steinert, T. Pertsch, H. Gross, M. Krause, J. Limpert, and J. Rothhardt, Material-specific high-resolution table-top extreme ultraviolet microscopy, Light Sci. Appl. **11**, 117 (2022).

[12] Y. Esashi, N. W. Jenkins, Y. Shao, J. M. Shaw, S. Park, M. M. Murnane, H. C. Kapteyn, and M. Tanksalvala, Tabletop extreme ultraviolet reflectometer for quantitative nanoscale reflectometry, scatterometry, and imaging, Rev. Sci. Instrum. **94**, 123705 (2023).

[13] B. Wang, N. J. Brooks, P. Johnsen, N. W. Jenkins, Y. Esashi, I. Binnie, M. Tanksalvala, H. C. Kapteyn, and M. M. Murnane, High-fidelity ptychographic imaging of highly periodic structures enabled by vortex high harmonic beams, Optica **10**, 1245 (2023).

[14] Y. Zhang, C. Murthy, T. R. Kafle, W. You, X. Shi, L. Min, H. H. Wang, N. Li, V. Gopalan, Z. Mao, K. Rossnagel, L. Yang, H. Kapteyn, R. Nandkishore, and M. Murnane, Bipolaronic nature of the pseudogap in quasi-one-dimensional $(TaSe_4)_2I$ revealed via weak photoexcitation, Nano Lett. **23**, 8392 (2023).

[15] A. L'Huillier, K. J. Schafer, and K. C. Kulander, Higher-order harmonic generation in xenon at 1064 nm: The role of phase matching, Phys. Rev. Lett. **66**, 2200 (1991).

[16] I. P. Christov, H. C. Kapteyn, and M. M. Murnane, Quasi-phase matching of high-harmonics and attosecond pulses in modulated waveguides, Opt. Express **7**, 362 (2000).

[17] L. G. Gouy, Sur une propriété nouvelle des ondes lumineuses, C. R. Acad. Sci. **110**, 1251 (1890).

[18] M. B. Gaarde, J. L. Tate, and K. J. Schafer, Macroscopic aspects of attosecond pulse generation, J. Phys. B **41**, 132001 (2008).

[19] C. M. Heyl, C. L. Arnold, A. Couairon, and A. L'Huillier, Introduction to macroscopic power scaling principles for high-order harmonic generation, J. Phys. B **50**, 013001 (2017).

[20] T. Tritschler, K. D. Hof, M. W. Klein, and M. Wegener, Variation of the carrier-envelope phase of few-cycle laser pulses owing to the Gouy phase: A solid-state-based measurement, Opt. Lett. **30**, 753 (2005).

[21] M. A. Porras, Characterization of the electric field of focused pulsed Gaussian beams for phase-sensitive interactions with matter, Opt. Lett. **34**, 1546 (2009).

[22] B. Major, D. Nemes, M. A. Porras, Z. L. Horváth, and A. P. Kovács, Carrier-envelope phase changes in the focal region: Propagation effects measured by spectral interferometry, Appl. Opt. **54**, 10717 (2015).

[23] D. Hoff, M. Krüger, L. Maisenbacher, A. M. Sayler, G. G. Paulus, and P. Hommelhoff, Tracing the phase of focused broadband laser pulses, Nat. Phys. **13**, 947 (2017).

[24] M. A. Porras, Z. L. Horváth, and B. Major, Three-dimensional carrier-envelope-phase map of focused few-cycle pulsed Gaussian beams, Phys. Rev. A **98**, 063819 (2018).

[25] Y. Zhang, D. Zille, D. Hoff, P. Wustelt, D. Würzler, M. Möller, A. M. Sayler, and G. G. Paulus, Observing the importance of the phase-volume effect for few-cycle light-matter interactions, Phys. Rev. Lett. **124**, 133202 (2020).

[26] R. Reiff, J. Venzke, A. Jaron-Becker, and A. Becker, Interference effects in harmonic generation induced by focal phase distribution, OSA Continuum **4**, 1897 (2021).

[27] B. Ghomashi, R. Reiff, and A. Becker, Coherence in macroscopic high harmonic generation for spatial focal phase distributions of monochromatic and broadband Gaussian laser pulses, Opt. Express **29**, 40146 (2021).

[28] X. Tang, B. Li, K. Wang, Z. Yin, C. Zhang, Z. Guan, B. Wang, C. D. Lin, and C. Jin, Role of the Porras factor in phase matching of high-order harmonic generation driven by focused few-cycle laser pulses, Opt. Lett. **48**, 3673 (2023).

[29] E. Karimi, C. Altucci, V. Tosa, R. Velotta, and L. Marrucci, Influence of generalized focusing of few-cycle Gaussian pulses in attosecond pulse generation, Opt. Express **21**, 24991 (2013).

[30] M. A. Porras, Z. L. Horvath, and B. Major, On the use of lenses to focus few-cycle pulses with controlled carrier–envelope phase, Appl. Phys. B **108**, 521 (2012).

[31] M. A. Porras, B. Major, and Z. L. Horvath, Carrier-envelope phase shift of few-cycle pulses along the focus of lenses and mirrors beyond the nonreshaping pulse approximation: The effect of pulse chirp, J. Opt. Soc. Am. B **29**, 3271 (2012).

[32] M. Balázs, Phase and polarization changes of pulsed Gaussian beams during focusing and propagation, Ph.D. thesis, Szeged University, 2017.

[33] V. Hanus, B. Fehér, V. Csajbók, P. Sándor, Z. Pápa, J. Budai, Z. Wang, P. Paul, A. Szeghalmi, and P. Dombi, Carrier-envelope phase on-chip scanner and control of laser beams, Nat. Commun. **14**, 5068 (2023).

[34] H. Bachau, E. Cormier, P. Decleva, J. E. Hansen, and F. Martín, Applications of B-splines in atomic and molecular physics, Rep. Prog. Phys. **64**, 1815 (2001).

[35] L. Argenti and R. Moccia, K-matrix method with B-splines: $\sigma_{n\ell}$, β_n and resonances in He photoionization below $N = 4$ threshold, J. Phys. B **39**, 2773 (2006).

[36] C. W. McCurdy and F. Martín, Implementation of exterior complex scaling in B-splines to solve atomic and molecular collision problems, J. Phys. B **37**, 917 (2004).

[37] C. Hernández-García, J. A. Pérez-Hernández, J. Ramos, E. C. Jarque, L. Roso, and L. Plaja, High-order harmonic propagation in gases within the discrete dipole approximation, Phys. Rev. A **82**, 033432 (2010).

[38] T. Joyce and A. Jaron-Becker, Macroscopic properties of high-order harmonic generation from molecular ions, Opt. Lett. **45**, 1954 (2020).